NANO · MICRO small
www.small-journal.com

Se-p Orbitals Induced "Strong d–d Orbitals Interaction" Enable High Reversibility of Se-Rich ZnSe/MnSe@C Electrode as Excellent Host for Sodium-Ion Storage

Sikandar Iqbal, Aadil Nabi Chishti, Muhammad Ali, Moazzam Ali, Youchan Hao, Xingxing Wu, Huiqin Huang, Wang Lu, Peng Gao, Muhammad Yousaf, and Yinzhu Jiang**

The heterostructure of transition-metal chalcogenides is a promising approach to boost alkali ion storage due to fast charge kinetics and reduction of activation energy. However, cycling performance is a paramount challenge that is suffering from poor reversibility. Herein, it is reported that Se-rich particles can chemically interact with local hexagonal ZnSe/MnSe@C heterostructure environment, leading to effective ions insertion/extraction, enabling high reversibility. Enlightened by theoretical understanding, Se-rich particles endow high intrinsic conductivities in term of low energy barriers (1.32 eV) compared with those without Se-rich particles (1.50 eV) toward the sodiation process. Moreover, p orbitals of Se-rich particles may actively participate and further increase the electronegativity that pushes the Mn d orbitals (dxy and dx^2-y^2) and donate their electrons to dxz and dyz orbitals, manifesting strong d–d orbitals interaction between ZnSe and MnSe. Such fundamental interaction will adopt a well-stable conducive electronic bridge, eventually, charges are easily transferred from ZnSe to MnSe in the heterostructure during sodiation/desodiation. Therefore, the optimized Se-rich ZnSe/MnSe@C electrode delivered high capacity of 576 mAh g^{-1} at 0.1 A g^{-1} after 100 cycles and 384 mAh g^{-1} at 1 A g^{-1} after 2500 cycles, respectively. In situ and ex situ measurements further indicate the integrity and reversibility of the electrode materials upon charging/discharging.

1. Introduction

Sodium-ion batteries (SIBs) have gained increasing attention as a cost-effective alternative to lithium-ion batteries (LIBs) for large-scale energy storage systems due to the homogenous and abundant supply of sodium (Na) on Earth.[1] However, the larger size and heavy mass of Na ions (1.06 Å and 23 g mol^{-1}) compared with Li^+ (0.76 Å and 6.9 g mol^{-1}), lead to sluggish kinetics and a higher potential barrier for ions insertion/extraction into active materials.[2] As a result, most of the electrode materials hardly maintain the resultant volume variations during discharging/charging process, significantly limiting the stability of the electrode materials.[3] Therefore, it is crucial to identify active materials with favorable sites for Na^+ ion diffusion and to understand the reaction mechanisms to overcome these challenges for the development of SIBs.

To date, various transitional metal selenides have garnered significant attention

S. Iqbal, A. N. Chishti, M. Ali, M. Ali, Y. Hao, X. Wu, H. Huang, M. Yousaf, Y. Jiang
ZJU-Hangzhou Global Scientific and Technological Innovation Center
Zhejiang University
Hangzhou 310027, China
E-mail: muhammadyousaf@zju.edu.cn; yzjiang@zju.edu.cn
S. Iqbal, A. N. Chishti, M. Ali, Y. Hao, X. Wu, H. Huang, Y. Jiang
School of Materials Science and Engineering
Zhejiang University
Hangzhou 310027, China
W. Lu
School of Material Science and Engineering
Shandong University
Jinan 250100, China
P. Gao
International Center for Quantum Materials and Electron Microscopy Laboratory, School of Physics
Peking University
Beijing 100871, China

The ORCID identification number(s) for the author(s) of this article can be found under https://doi.org/10.1002/smll.202308262

DOI: 10.1002/smll.202308262

as electrode materials for SIBs due to their unique properties, including excellent intercalation and deintercalation capabilities.[4] Among them, ZnSe, $CoSe_2$, $MoSe_2$, WSe_2, $FeSe_2$, and MnSe, all have shown promise in Na ion insertion/extraction processes.[5] Furthermore, bimetallic selenide heterostructures portray great synergistic significance in term of cyclability, such as $CoSe_2/FeSe_2$,[6] MoS_2/Bi_2S_3,[7] $ZnSe/CoSe_2$,[8] and $FeSe_2/Fe_3Se_4$,[5d] have corroborated popular in the field of synthetic materials due to their ability to facilitate redox reactions during discharging and charging processes. However, these heterostructures can decrease the electronic conductivity due to the presence of different metals with different electronegativity and may be difficult to tune the movement of electrons across the material. As a result, the weak d–d coupling of metal orbitals in the heterostructures can build a weak metallic bond due to the mismatching of electronic band structures. This can cause trapped electrons in the interface defect, resulting in high polarization, decreasing the overall electrochemical performances.[9]

To overcome these limitations, on one side the researchers measure the systematic control of morphology, size, and coating which are the propitious strategies.[5a,10] On the other hand, they are also making sufficient efforts in terms of various dopants, vacancies and rich concentrations of O_2, N, P, S, and Se with heterostructures to boost the reaction kinetics.[11] However, there are few studies available to well explain the intrinsic electronic crystal structure responsible for high electronic conductivity during the cycling process and remains elusive. In contrast, the electronic transportation of metal chalcogenides with ultra-narrow bandgaps have intrinsic bandgaps close to zero and can exhibit metal-like behavior when the bandgap is sufficiently narrow. As is widely acknowledged the narrow bandgap means that the material has high conductivity, which is more likely to exhibit high-rate performance of the material.[12] Besides, the electronegativity of the partially filled d-orbitals also plays a crucial role during the binary metal d–d orbitals coupling, which means that stronger electronegativity will make a highly conducive path for electrons transportation during ions insertion/de-insertion process, bestowing high reversibility.[13] Following the Sabatier principle, the Zn and Mn nodes present a completely filled and half-empty d-orbitals, which results in establishing d–d coupling that is either too weak or too strong. To the best of our observation, the Se-rich ZnSe/MnSe@C heterostructures for SIBs remain a big challenge. This related topic lacks the necessary in-depth investigation to facilitate modulating electronic structures of metal nodes to profoundly improve battery performance.

Drawing inspiration from the aforementioned considerations, we proposed a competitive coordination strategy to synthesize Se-rich ZnSe/MnSe@C heterostructures. Our optimized 2D hexagonal nanocomposite is well decorated with Se-rich particles that cannot only impart tensile strength to its hexagonal shape but also enhance the overall electrode material conductivity during cycling processes. These Se-rich particles directly attach to the ZnSe crystal in the heterostructure, which has a higher electronegativity compared to the composite without Se-rich particles. The key role of these Se-rich particles is to establish a stable coordination bridge through the strong d–d interaction of Zn and Mn orbitals. There are two critical concepts involved, first the filled d-eg orbitals (dx^2-y^2 and dxy) of the Zn display diamagnetic behavior when they come close to the conduction band, second the unfilled d-t_2g orbitals (dz^2-xz and dyz) of the Mn exhibit paramagnetic behavior when they are away from the conduction band. In further context, the density functional theory (DFT) revealed that the unfilled Mn d orbitals (dxy and dx^2-y_2) donate their electrons to dxz and dyz, pushed by Se-rich p-orbitals, resulting in a shift from paramagnetic (high spin) to ferromagnetic (low spin) state. This generates strong interaction between d–d orbitals of Zn and Mn, facilitating charge transfer from ZnSe to MnSe, providing ample sites for highly Na ions insertion/de-insertion and relieving volume expansion which in turn enhances the reversibility of the electrode materials during cycling. The in situ XRD, ex situ EIS, HRTEM, and in-depth DFT investigations verified the electrochemical conversion mechanism responsible for performance enhancement. These critical Se-rich as well as strong d–d coupling orbitals base electrode materials pave the way for a better understanding of the high insertion/de-insertion of Na ions which further enhances the cycling performance.

2. Results and Discussion

2.1. Theoretical Understanding

The band structure of Na-based transitional metal selenides heterostructures simply considers orbital overlaps between the transitional metal d orbitals and selenide p orbitals resulting in bonding (M—Se) and antibonding (M—Se)* bands having strong ligand and metal characters, respectively. The energy difference between (M—Se) and (M—Se)* also called the charge transfer depends on the electronegativity differences of M and Se.[14] In addition, in the case of heterostructures, the charge is transferred through d–d interaction, the higher the electronegativity difference will stronger the d–d interaction, resultantly will obtain a stronger metallic bond. These electrons move across the lattice forming states on certain sites with doubly occupied d orbitals and empty orbitals on other sites.[6] The Se-rich environment further increases the electronegativity, suggesting that the orbitals lie near the Fermi level and may surpass the strong electronic overlapping. To determine the relationship of the band structures with reversibility, we investigate the typical Se-rich ZnSe/MnSe@C heterostructure which can enable high performance during the Na ions insertion/de-insertion process as shown in schematic model 1. In this work, we synthesized five different kinds of heterostructures through different temperature conditions, such Se-rich heterostructures were produced at 600, 700, and 800 °C, whereas without Se-rich heterostructures were achieved at 400, 500 °C, and the as optimized 600 °C Se-rich composite was further explored to find the correlation between d–d interaction and highly conversion of Na_2Se.

Typically, in the heterostructures, the charge will transfer from ZnSe to MnSe due to the electronegativity difference. It is worth noting, that the ZnSe of the Se-rich base heterostructure shows higher electronegativity compared with simple heterostructure, due to the Se-rich environment which will not only accelerate the charge transformation from ZnSe to MnSe in the heterostructure but will also establish strong d–d interaction between metal orbitals as shown in **Figure 1a**. Indeed, we also found that the distance between t_2g and eg orbitals of Mn is quite lower in Se-rich composite.[15] These types of excited

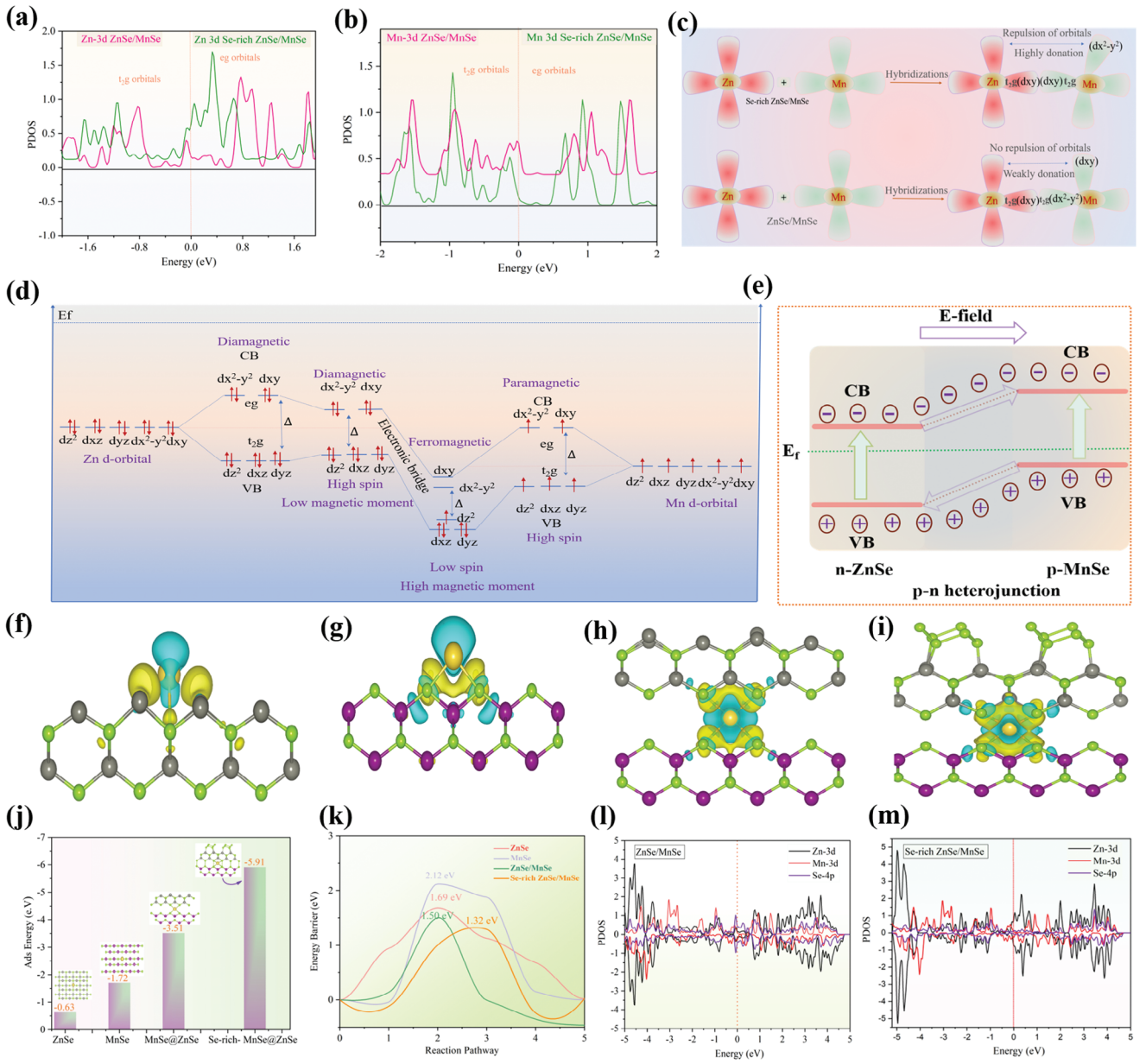

Figure 1. a,b) PDOS of Zn and Mn 3d orbitals, c) schematic illustration of Zn and Mn orbitals hybridization with and without Se-rich ZnSe/MnSe composites, d) MOT schematic d–d orbitals splitting of Zn and Mn, e) p–n heterojunction schematic illustration, f–i) optimized charge density models, j) adsorption energies, k) energy barriers of ZnSe, MnSe, ZnSe/MnSe, and Se-rich ZnSe/MnSe, l,m) PDOS of both ZnSe/MnSe, and Se-rich ZnSe/MnSe, respectively.

configurations correspond to the strong coupling and repulsion of Zn and Mn orbitals, which are envisioned to form the physical band edges for a high donation of electrons (Figure 1b,c). Therefore, we present the overall band structure of the heterostructure followed by using the molecular orbitals theory (MOT) diagram (Figure 1d), on the left side all the Zn d orbitals are filled that show diamagnetic behavior, high spin, and low magnetic moment while the right-side Mn d orbitals are partially filled shows paramagnetic behavior, low spin, and high magnetic moment. It is worth noting, that due to the Se-rich particles the Zn metal in the heterostructure has obtained higher electronegativity compared with that simple heterostructure and pushes the electrons of Mn orbitals (from t_2g to eg). We also carried out magnetic moment experimentally, and optimized Se-rich ZnSe/MnSe@C heterostructure exhibits higher magnetic moment (Figure S1, Supporting Information). As a result, the Mn eg orbitals become empty and may further shift from a paramagnetic to a ferromagnetic state, implying low spin and high magnetic moment.[16] This separation between low spin and high spin forms a very successful exchange through the electronic bridge, suggesting that the heterostructure will favorably transfer electrons from ZnSe to MnSe. This simply means that the Na ions will be highly

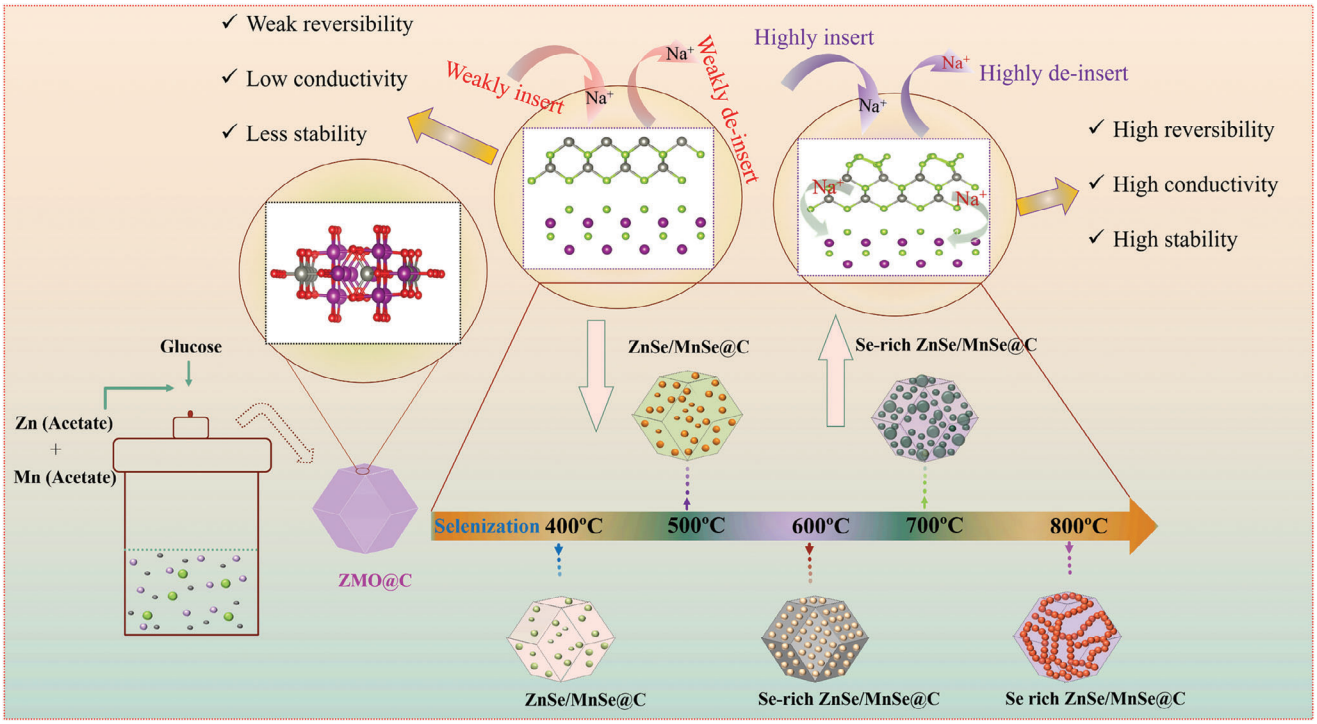

Scheme 1. Schematic illustration of Se-rich ZnSe/MnSe@C heterostructures obtained at different temperatures (400, 500, 600, 700, and 800 °C) during the selenization process.

inserted/deinserted in the heterostructure during discharging and charging process which will not only increase the reversibility in term of immense conversion of redox reaction but will also improve the long cycling performance of the electrode materials.[7] Furthermore, the PDOS deeply insight the band structures of Zn and Mn orbitals, respectively, as shown in Figure 1e,f and Figure S2 (Supporting Information), and the PDOS after Na ions insertion is shown in Figure S3 (Supporting Information). Figure 1g represents the schematic diagram that the charge will transfer from n-type ZnSe to p-type semiconductor (MnSe) in the p–n heterojunction during the Na ions insertion/de-insertion process. Interestingly, the Zn (e.g., orbitals) of the Se-rich composite are near to Fermi level (conduction band) whereas Mn (e.g., orbitals) are away from the conduction band, representing the strong interaction between d–d orbitals. To further verify the crucial role of Se-rich composite in terms of superior Na^+ diffusion kinetics, we have optimized the crystal structures of the ZnSe, MnSe, ZnSe/MnSe, and Se-rich ZnSe/MnSe, before and after Na ions intercalation/deintercalation process, respectively (Figures S4–S6, Supporting Information). Figure 1f–i illustrates the optimized electronic structures along with charge density in which the charge accumulation (cyan part) and charge depletion (yellow part) disclosed the charge transfer from Na^+ to the samples. The charge accumulation region of the Se-rich composite was not only observed in between the Na atom and ZnSe/MnSe but also showed less inter-layer distance between ZnSe and MnSe heterointerfaces that is considered for stable heterostructure, suggesting the strong binding energy of Na^+ and Se-rich composite. As expected the highest adsorption energy (E_{ads}) of Na^+ in the Se-rich composite were computed, −5.91 eV compared with ZnSe/MnSe, ZnSe and MnSe of −3.51, −0.63, and −1.72 respectively (Figure 1j). It is demonstrated here that the Se-rich particles can improve the Na^+ adsorption ability of ZnSe/MnSe for high ion storage capacity. It is widely known that the electrochemical performance of SIBs is highly correlated with the ion migration energy barrier.[17] Figure 1k depicts the Na ion diffusion path and energy barriers on these four systems using the climbing image nudged elastic band method. The diffusion energy barrier of the Se-rich composite (1.32 eV) was much lower than those of ZnSe/MnSe (1.50 eV), ZnSe (1.69 eV), and MnSe (2.12 eV), indicating that the Na^+ is energetically more favorable in Se-rich composite. The density of states (DOS) calculation was computed for ZnSe, MnSe, ZnSe/MnSe, and Se-rich ZnSe/MnSe composites before and after Na ions to obtain the electrical properties. The Se-rich particles led to an increase in DOS for ZnSe/MnSe, as can be seen from the density differences at the Fermi level in Figure 1l,m. This suggests that compared to semiconducting ZnSe/MnSe, conducting Se-rich ZnSe/MnSe composites can exhibit significantly higher electrical conductivity. Overall, these calculation results suggest that the Se-rich particles can significantly increase the electrical conductivity and ion transport/adsorption capacity of the ZnSe/MnSe anode.

2.2. Physical Characterizations

The synthetic route of Se-rich ZnSe/MnSe@C heterostructure is illustrated in **Scheme 1**. Initially, the ZMO@C was prepared through a hydrothermal process and then followed by a

solid-state reaction at different temperatures (400, 500, 600, 700, and 800 °C) in the presence of Se powder. Simple ZnSe/MnSe@C heterostructures (i.e., without Se-rich particles) were obtained at 400 and 500 °C, while Se-rich ZnSe/MnSe@C heterostructures were produced at 600, 700, and 800 °C. The as optimized Se-rich ZnSe/MnSe@C heterostructure was achieved at 600 °C, which inevitably leads to the uniform decoration of Se particles. The scanning electron microscopy (SEM) and transmission electron microscopy (TEM) images unveil the morphology transformation from the smooth surface of hexagonal shape ZMO@C to Se-rich decorated hexagonal composites (**Figure 2**a–f; Figures S7–S11, Supporting Information). It is worth noting that the uniform decoration of Se-rich particles with equal size (about 18–20 nm) on the ZnSe/MnSe@C hexagonal shape favorable governing the electrochemical performances, including high insertion of Na ions during discharging/charging, high intrinsic conductivity and cyclability of the electrode materials are due to its crystal structure advantages. In contrast, at 700, and 800 °C has also obtained Se-rich base heterostructures in which Se-rich particles are unequal in size but also forming clusters which may further deteriorate conductivity, and ultimately suppress the electrochemical performances. Furthermore, the high-resolution TEM (HRTEM) image illustrates the uniformly decorated nano-size Se-rich particles which are about 18–20 nm, and the crystal lattice fringes of all components are separated via heterointerfaces (Figure 2g,h). The Se-rich particles correspond to a crystal lattice plan of (100), while (220) and (111) are associated with ZnSe and MnSe, respectively (Figure 2i–l). The inverse FFT may orderly support the crystal lattice plans. The homogenous distribution of Zn, Mn, Se, and C over the entire heterostructure is confirmed by energy-dispersive X-ray spectroscopy (Figure 2m). It is important to note, that the elemental mapping of Se is quite brighter than other elements representing the existence of Se-rich in the architecture.

The X-ray diffraction patterns (XRD) of Se-rich ZnSe/MnSe@C heterostructure are depicted in Figure S12a (Supporting Information), all the diffraction peaks are well indexed with both cubic phase of ZnSe (space group of F-43(216), JCPDS# 37–1463) and the cubic phase of MnSe (F-43(216), JCPDS# 27–0311), which further confirm the presence of ZnSe and MnSe in the hybrid structure, implying that homogeneous cubic phases of both metals are preferable than heterogeneous phases in bimetallic heterostructures.[18] In addition, the Se-rich particles in the as optimized heterostructure are recognized with JCPDS# 51–1389. The XRD of different heterostructures are illustrated in Figure S12b (Supporting Information), at 400 °C No peaks were observed for Se-rich particles, but weak peaks were obtained for Se-rich at 500 °C, and they become more prominent at 600 °C, suggesting the Se-rich particles as a part of the heterostructure, although the peaks obtained for 700 and 800 °C with high intensity, however, the size and decoration may influence the electronic conductivity. Therefore, the heterostructure obtained at 600 °C is ideal among all heterostructures. Furthermore, it is critical to note that in the conventional ZnSe/MnSe@C heterostructure, ZnSe has significantly higher peak intensities than MnSe, implying that electrons or ions can flow more easily from ZnSe to MnSe than other heterostructures.[6] The Raman spectra show the peaks at 180, 565 cm^{-1} and 663, 240 cm^{-1} indicating existence of ZnSe and MnSe (Figure S13, Supporting Information), while the D band and G band reside at 1325 and 1579 cm^{-1} show the presence of carbon in the composites, respectively.[19,20] Moreover, the optimized composite also confirms a high insensitivity ratio of the G and D-bands, having a considerable degree of disorder and defects in nanocomposites, suggesting a significant role in ion transportation. The detailed surface composition and elemental states of ZnSe/MnSe@C heterostructures were measured through X-ray photoelectron spectroscopy analysis and explanation is provided in Supporting Information (Figures S14,S15, Supporting Information).

The chemical changes and carbon content of Se-rich ZnSe/MnSe@C heterostructure were observed through thermogravimetric analysis (TGA) with the temperature ranging from 30 to 600 °C in air (Figure S12c, Supporting Information). The 0.5 wt.% weight loss ranging from 30–450 °C can be attributed to the elimination of free water and physically absorbed water in the air. Beyond that, the weight loss of 36.1% between 450 and 470 °C could be ascribed to the elimination of Se-rich particles and carbon residues, while the weight loss onward from 470 to 550 °C is due to the oxidation of composite materials (ZnSe was transformed to ZnO, Se, and MnSe was transformed into MnO or MnO_2).[21] The porous structure and surface area of the Se-rich ZnSe/MnSe@C heterostructure were investigated through N_2 adsorption/desorption analysis (Figure S12d, Supporting Information). The as optimized nanocomposite has a larger surface area of 215 $m^2\ g^{-1}$ with an average pore size distribution of 0.4–10 nm, indicating a micro-mesoporous structure. With such a suitable structure and surface area, the electrode/electrolyte can form a sustainable connection that not only relies on volume expansion during cycling but also adequate pseudocapacitive behavior, hence increasing Na ion storage.[19]

2.3. Electrochemical Performance

In general, the structural evolution will enhance the performance of batteries in term of high reversibility. Three CV (cyclic voltammetry) cycles were employed within the potential range (V versus Na/Na^+) of 0.01–3.0 V to understand the Na ion insertion/deinsertion mechanism in the optimized Se-rich ZnSe/MnSe@C heterostructure (**Figure 3**a). Initially, two small cathodic peaks were observed at 2.25 and 1.98 V, respectively which are attributed to the insertion of Na^+ into the Se-rich ZnSe/MnSe@C. Meanwhile, two broad peaks were obtained at 1.07 and 1.25 V for an anodic sweep that corresponded to deinsertion of Na^+ from the Se-rich ZnSe/MnSe@C. During the following cycles, the distinct peaks at ≈0.60/1.12 V coincided with conversion reactions between MnSe and Mn/Na_2Se, while a couple of peaks at ≈0.11/0.90 V may attribute to the conversion of ZnSe to Zn/Na_2Se. It is well known, that after the initial cycle, these CV profiles overlap well, demonstrating the remarkable reversibility and cyclic stability during cycling process. It is worth noting, that the separation of the peaks at a lower potential can make it easier for the Na ions to insert into the electrode material and thus promote a reversible reaction. This is because a lower potential means that less energy is required to move the Na ions into and out of the electrode material. Therefore, the as-obtained optimized Se-rich

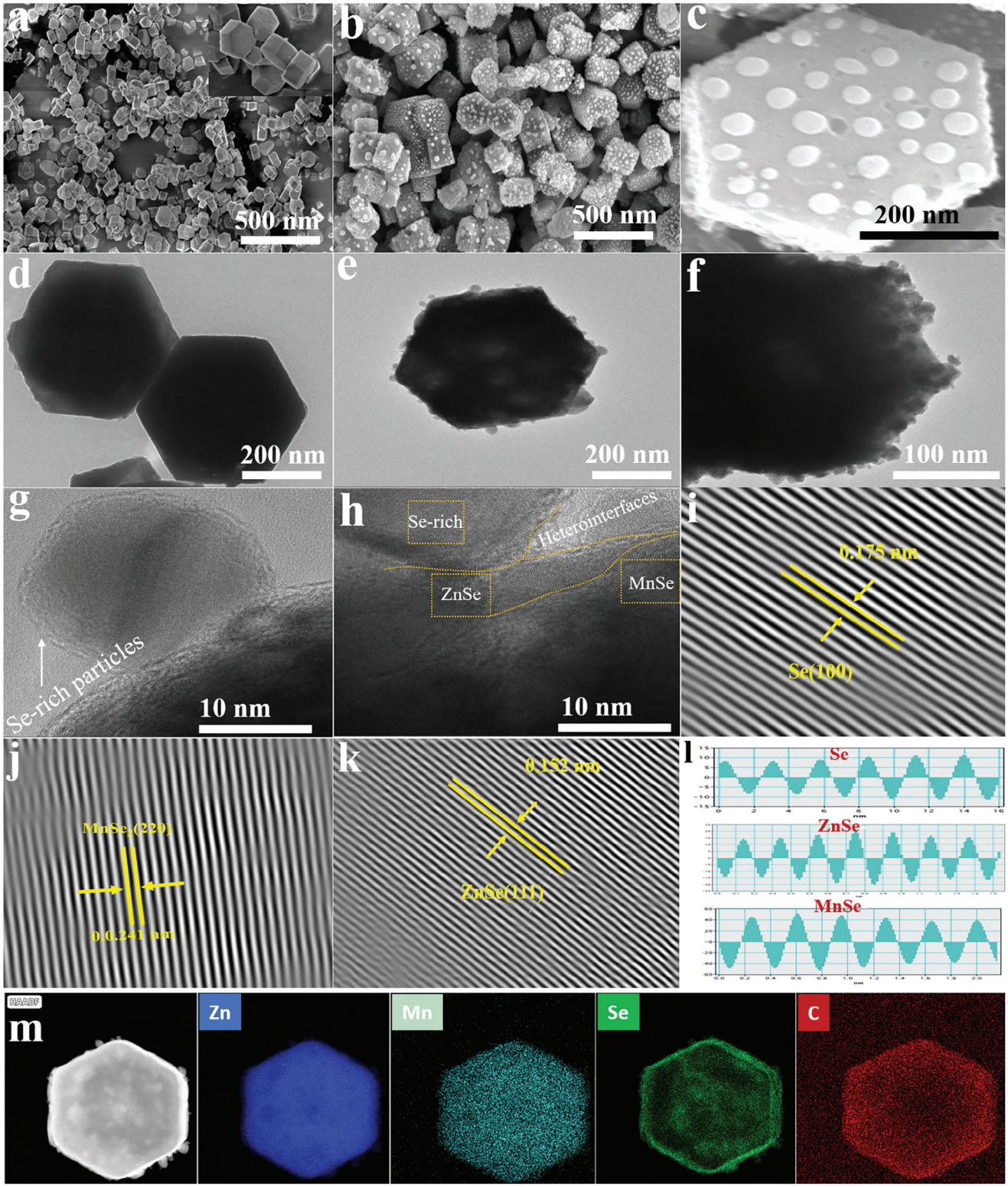

Figure 2. Structural and morphological analysis: a–c) FESEM images of the optimized Se-rich ZnSe/MnSe@C heterostructure. d–f) TEM, g,h) HRTEM images, i–l) inverse FFT images and m) the elemental mapping for Zn, Mn, Se, and C of the optimized Se-rich ZnSe/MnSe@C heterostructure.

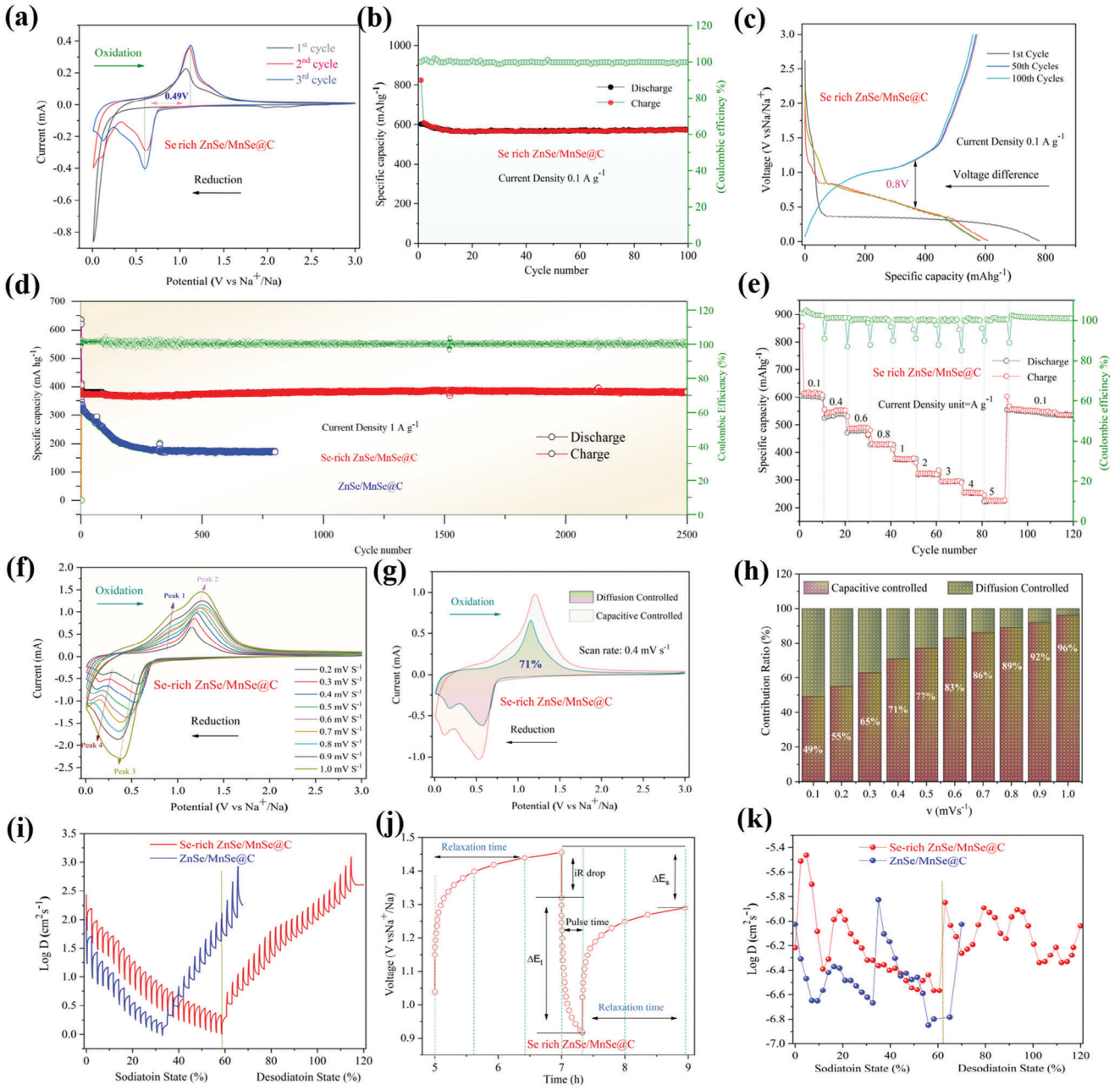

Figure 3. Electrochemical performances. a) Three CV curves at scan rate 0.1 mV S^{-1}. b) Cycling performances, c) galvanostatic discharge and charge profiles, d) long cycling performances, and e) rate the performance of the Se-rich ZnSe/MnSe@C. f) CV at different scan rates. g) Capacitive contribution at 0.4 mV s^{-1} scan rate of Se-rich ZnSe/MnSe@C. h) pseudocapacitive contribution proportion at different scan rates of Se-rich ZnSe/MnSe@C heterostructure. GITT analysis, i) GDC curves in term of sodiation and desodiation, j) unite curve of the GITT curve of the Se-rich ZnSe/MnSe@C electrode, and k) D_{Na+} value of the optimized process of Se-rich ZnSe/MnSe@C electrode and ZnSe/MnSe@C.

ZnSe/MnSe@C heterostructure has relatively smaller CV peak separations (≈0.49 V) than those of previously reported Cu_2Se,[22] Mn-Fe-Se/CNT,[18b] and CoSe-CuSe,[23] indicating its higher intrinsic conductivity (As smaller peak separation values closely related to low polarization of the electrode materials). As a result, it is assumed that Se-rich particles that are uniformly decorated on the surface of Se-rich ZnSe/MnSe@C can significantly contribute to the high conductivity of the entire electrode materials, signifying the important point for highly efficient electrochemical conversion reactions. The related Na^+ insertion/deinsertion reactions may undergo multiple stages. The overall detailed conversion and alloying/dealloying mechanism equations are as follows:[8]

Conversion reaction:

$$Na_x\ ZnSe\ +\ (2-x)\ Na^+ +\ (2-x)\ e^-\ \leftrightarrow\ Na_2Se\ +\ Zn \qquad (1)$$

$$xNa^+ + ZnSe + xe^- \leftrightarrow Na_x ZnSe \quad (2)$$

$$MnSe + x\,Na^+ + xe^- \leftrightarrow Na_x MnSe \quad (3)$$

$$Na_x MnSe + (2-x)\,Na^+ + (2-x)\,e^- \leftrightarrow Na_2Se + Mn \quad (4)$$

$$Se + 2\,Na^+ + 2e^- \leftrightarrow Na_2Se \quad (5)$$

Alloying/dealloying reaction:

$$13\,Zn + Na^+ + e^- \leftrightarrow NaZn_{13} \quad (6)$$

The significant cycling performances of various electrodes (such as ZnSe@C, MnSe@C, ZnSe/MnSe@C-400 °C, ZnSe/MnSe@C-500 °C, Se-rich ZnSe/MnSe@C-600 °C, Se-rich ZnSe/MnSe@C-700 °C, and Se-rich ZnSe/MnSe@C-800 °C) are compared in Figure 3b and Figures S16–S18 (Supporting Information), and superior cycling performance was achieved with Se-rich ZnSe/MnSe@C-600 °C composite. The battery using Se-rich ZnSe/MnSe@C-600 °C achieves astonishing high first discharge and charge capacity of 930/720 mAh g^{-1} at 0.05 A g^{-1} (Figure 18b, Supporting Information) and 780/619 mAh g^{-1} at 0.1 A g^{-1}, (Figure 3b) with high initial coulombic efficiency (ICE) of 77% and 79%, respectively. Initially, the electrode lost the capacity in the very first cycles which could be attributed to the decomposition of electrolyte as well as the formation of the SEI layer, while the electrode exhibits stable coulombic efficiency (CE) with cycles. Additionally, we also further optimized the electrolyte using Se-rich ZnSe/MnSe@C-600 °C electrode. The electrolyte $NaClO_4$ dissolved in PC (polyethylene carbonate) and DEC (diethylene carbonate) 2:1 revealed the highest ICE of 79% compared with other electrolytes (Figure S19, Supporting Information), indicating a thin and robust SEI layer. The as-expected electrode will not only enhance the intrinsic conductivity and fasten the electrochemical conversion reaction but will also prevent it from severe volume expansion during the cycling process. The typical galvanostatic discharge and charge curves of Se-rich ZnSe/MnSe@C electrode for different cycles (1st, 50th, and 100th) at 1.0 A g^{-1} are shown in Figure 3c. As we can see the GDC curves are very close and almost overlapped on each other representing outstanding cyclability of the material. Impressively, when the Se-rich ZnSe/MnSe@C electrode was subjected to prolonged cycling at 1 A g^{-1}, the specific capacity was obtained of 384 mAh g^{-1} with ≈100% CE after 2500 cycles (Figure 3d), and still capacity of ≈203 mAh g^{-1} after 700 cycles was attained even at ultra-high current density of 10 A g^{-1}, indicating stable structure of electrode even after several cycles. (Figure S18a, Supporting Information). In comparison, the long cycling performance of the ZnSe/MnSe@C electrode is inferior to Se-rich ZnSe/MnSe@C (Figure S20, Supporting Information). Thus, it indicates that the richness of Se at 600 °C is optimized to facilitate rapid electron/ion transfer, leading to highest electrochemical activity and Na^+ storage. Upon cycling, Se-rich ZnSe/MnSe@C-600 °C delivers average capacities of 604, 496, 401, 389, 370, 364, 351, 343, and 291 mAh g^{-1} at increasing rate of 0.2, 0.4, 0.6, 0.8, 1.0, 1.5, 2.0, 2.5, and 3.0 A g^{-1}, respectively. Interestingly, when the current density reverted to 0.1 A g^{-1} the electrode still presented its original capacity, suggesting rapid delivery of ions or electrons. In addition, our work shows superior performance compared with most of reported selenide based materials (Table S2, Supporting Information).

We have also carried out ex situ SEM after several cycles and after cycling to observe the electrode integrity and volume expansion of the Se-rich ZnSe/MnSe@C and ZnSe/MnSe@C as shown in (Figure S21, Supporting Information). The Se-rich electrode maintains the structural integrity during the cycling process, which may benefit the strong reversibility of the electrode materials as shown in (Figure S21a–c, Supporting Information). The volume expansion exhibited by the Se-rich ZnSe/MnSe@C electrode (≈5.4 µm) illustrated in Figure S21d–f (Supporting Information) is notably lower than that of the ZnSe/MnSe@C electrode (≈11.5 µm, Figure S21g–i, Supporting Information). Furthermore, we also carried out the SEM and TEM after prolonged cycling which shows the high integrity of the electrode materials (Figure S21, Supporting Information). It is worth noting, that the high integrity and lower volume expansion of the Se-rich ZnSe/MnSe@C electrode manifest superb electrochemical performance compared with those without Se-rich particle heterostructures. These robust and remarkable electrochemical performances of the Se-rich ZnSe/MnSe@C-600°C electrodes may frequently be attributed to the unique decoration of Se-rich particles on ZnSe/MnSe@C hexagonal shape which may provide structural support to the electrode and prevent it from severe volume expansion and pulverization, implying admirable cycling performance.

To understand better performance of Se-rich composite than that without Se-rich, CV curves at different scan rates are made (Figure 3f; Figure S24a, Supporting Information). Both the oxidation and reduction curves are well preserved, but a minute cathodic peak toward negative shift and a slightly anodic peak toward positive shift corresponding to low polarization at higher scan rate.[24] The key reasons for enhanced rate capability compared to other electrodes are mainly associated with increased capacitive contribution and improved ion diffusion kinetics, which means that the optimized electrode will present a faster Na^+ diffusion rate. To identify the electrochemical reaction behavior (diffusion-controlled or surface capacitive) the power law was used to calculate the relationship between ($i = av^b$) current response (i) and scan rate (v), whereas the b value is typically indicative of charge storage mechanism. The b value for the two redox peaks is 0.74, 0.91, 0.89, and 0.78, respectively, which are >0.5, indicating that the electrochemical kinetics of Na ion storage is predominantly controlled by the surface capacitance (Figure S23, Supporting Information). The Se-rich ZnSe/MnSe@C-600 °C electrode demonstrates a capacitive contribution of ≈71% at 0.4 mV s^{-1} (Figure 3h), while Figure 3k displays the pseudocapacitive contribution proportion at different scan rates. The quantitative analysis reveals that the capacitive contribution improves with increasing scan rates, and thus obtained the highest pseudocapacitive contribution of ≈96% at a sweep rate of 1 mV s^{-1}. In contrast, the pseudocapacitive contribution ratio of ZnSe/MnSe@C is lower than that of Se-rich ZnSe/MnSe@C (Figure S24, Supporting Information). Furthermore, the GITT characterizations gain a more profound comprehension of the ionic diffusion coefficients and the swift sodium ion storage behavior of Se-rich ZnSe/MnSe@C and ZnSe/MnSe@C composites. The galvanostatic discharge and charge patterns were observed during the desodiation and sodiation processes, as

depicted in (Figure 3i). The electrode initially activated for several cycles at 150 mA g^{-1} within a voltage window of 0.01–3.0 V. After activation, the battery underwent discharge and charge cycles at 120 mA g^{-1} for a duration of 20 min, followed by maintaining the battery at a steady voltage to attain equilibrium. This behavior was evident throughout the complete discharge (0.01 V) and charge (3.0 V) cycles. The intricate details of this phenomenon are illustrated by a representative GITT curve of the Se-rich ZnSe/MnSe@C electrode, depicted in Figure 3j, elucidating the underlying work mechanism during the GITT investigation. Notably, the minimal potential fluctuation during relaxation underscores the rapid migration of sodium ions. To quantify this phenomenon, Figure 3k showcases the Na^+ diffusion coefficients (D_{Na+}) derived from each pulse, with their values recorded during both sodiation and desodiation, as calculated using the following equation.

$$D^{GIIT} = \frac{4}{\pi\tau}\left(\frac{m_B V_m}{M_B S}\right)^2 \left(\frac{\Delta E_S}{\Delta E_\tau}\right)^2 \quad (7)$$

This equation (Equation (7)) describes, that the surface area and pulse time of the electrode at constant current are noting with S (cm^2) and τ (s) shows the parameters in terms of M_B (gm mol^{-1}) is the molecular weight of electrode, V_m (cm^3 mol^{-1}) is the molar volume, and m_B (g) is the active mass of the electrodes, respectively. The precise form of the above equation can be also written as:

$$D^{GIIT} = \frac{4L^2}{\pi\tau}\left(\frac{\Delta E_S}{\Delta E_\tau}\right)^2 \quad (8)$$

In the unite part of the GITT curve, ΔE_τ represents the voltage variations during constant pulse time except for iR drop and the two consecutive discharge pulse denoted as ΔE_s (V), which represents the steady state variation. The D_{Na+} value of the optimized Se-rich ZnSe/MnSe@C electrode is higher than those of the ZnSe/MnSe@C electrode, respectively, which ultimately creates an abundance of active sites for electrolytes and is capable of high Na ions storage.[25] The Se-rich ZnSe/MnSe@C electrode shows lower electron transfer resistance than those of ZnSe/MnSe@C.

2.4. Reaction Mechanism

To acquire the structural evolution during the Na ions insertion/deinsertion process, in situ, XRD, ex situ HRTEM, and simulation study were employed to investigate the reaction mechanism of the optimized Se-rich ZnSe/MnSe@C composite (**Figure 4**). The overall structural evolution of peak intensities of the XRD patterns for two consecutive cycles is illustrated in a counter plot in Figure 4a–e. Once the sodiation starts in the very first cycle, the XRD peaks for pristine composite are identified at 25.0°, 26.6°, and 45.6° corresponding to ZnSe (111), MnSe (111), and ZnSe (220), respectively. After continuously discharging the pristine peaks become weaker and weaker, gradually disappearing when the electrode becomes totally discharged to 0.01 V, and merges with new peaks at 22.1° and 36.8° which might be attributed to Na_2Se (111) and $NaZn_{13}$ (422). These variations further verify that the Na ions are inserted in (Na_xZnSe/MnSe). Upon the charging process, these peaks are again peaks that could be observed for oxidative reactants after when the electrode reaches to the maximum voltage value of 3.0 V. Although the peaks for ZnSe and MnSe are recycled with low crystallinity after the negligible charging process, but in the following cycle we can observe the peak variations of Na_2Se (111) and $NaZn_{13}$ (422), respectively, manifesting the highly reversible behavior of Se-rich ZnSe/MnSe@C electrode. Furthermore, ex situ HRTEM was also conducted to intrinsically measure the as obtained structural evolution of (Na_2Se, $NaZn_{13}$, and Mn) at a full discharge position of 0.01 V and charge position of 3.0 V (Figure 4g,h). A very clear d spacing during discharging process of 0.127, 0.198, and 0.233 nm are corresponding to Na_2Se (111), $NaZn_{13}$ (422), and Mn (101), while the d spacing of 0.240, 0.249, and 0.148 nm are attributed to ZnSe (111), ZnSe (220), and MnSe (111), respectively. To investigate more clearly, the simulation study may further signify the reversible redox process in term of low adsorption energies during insertion/deinsertion process (Figure 4f). These results are also consistent with our DFT calculations which are discussed in the above Figure 1. It is concluded here, that the Se-rich particles would help to assist more Na ions inside the ZnSe/MnSe@C composite and the electrode materials will show less resistance toward Na ions insertion/deinsertion process, implying high reversibility and low volume expansion. To get deep insight, we compare the excellent kinetics reaction of Se-rich ZnSe/MnSe@C with that of without Se-rich composites through ex situ electrochemical impedance spectroscopy (EIS) as shown in (Figures S25,S26, Supporting Information). The charge transfer resistance between electrode and electrolyte interface and Na^+ diffusion resistance in the electrode was measured through Nyquist low frequency slopping and high frequency semicircle line plots in a half cell. As illustrated in (Figure S25, Supporting Information), the electrode has significant resistance in the initial cycle due to the formation of a thick and irreversible SEI layer, but when continually discharged to 0.01 V, it shows less resistance than other discharging positions. More importantly, when the electrode is fully charged to 3.0 V, manifests lower charge resistance. These charge resistances are lower than those without Se-rich composites during the initial discharging and charging process, implying the formation of a thin reversible SEI layer in which the Na ions will be highly inserted/deinserted during the cycling process. In addition, we also further verify the thin SEI layer through EIS after prolonged cycling (Figure S27, Supporting Information). The electrode exhibits higher resistance during fewer cycles, while showing less resistance after prolonged cycling, manifesting thin and stable SEI layer formation during cycling process. The optimized electrolyte may also further help to obtain a stable and thin SEI layer as displayed in the schematic (Figure S28, Supporting Information).

2.5. Full Cell Performance

A full battery with Na vanadium phosphate ($Na_3V_2(PO_4)_3$, NVP) cathode to verify the practical application of Se-rich ZnSe/MnSe@C anode is demonstrated in (**Figure 5**). NVP is a conventional cathode and has obtained excellent performance especially when coupled with transitional metal selenides and

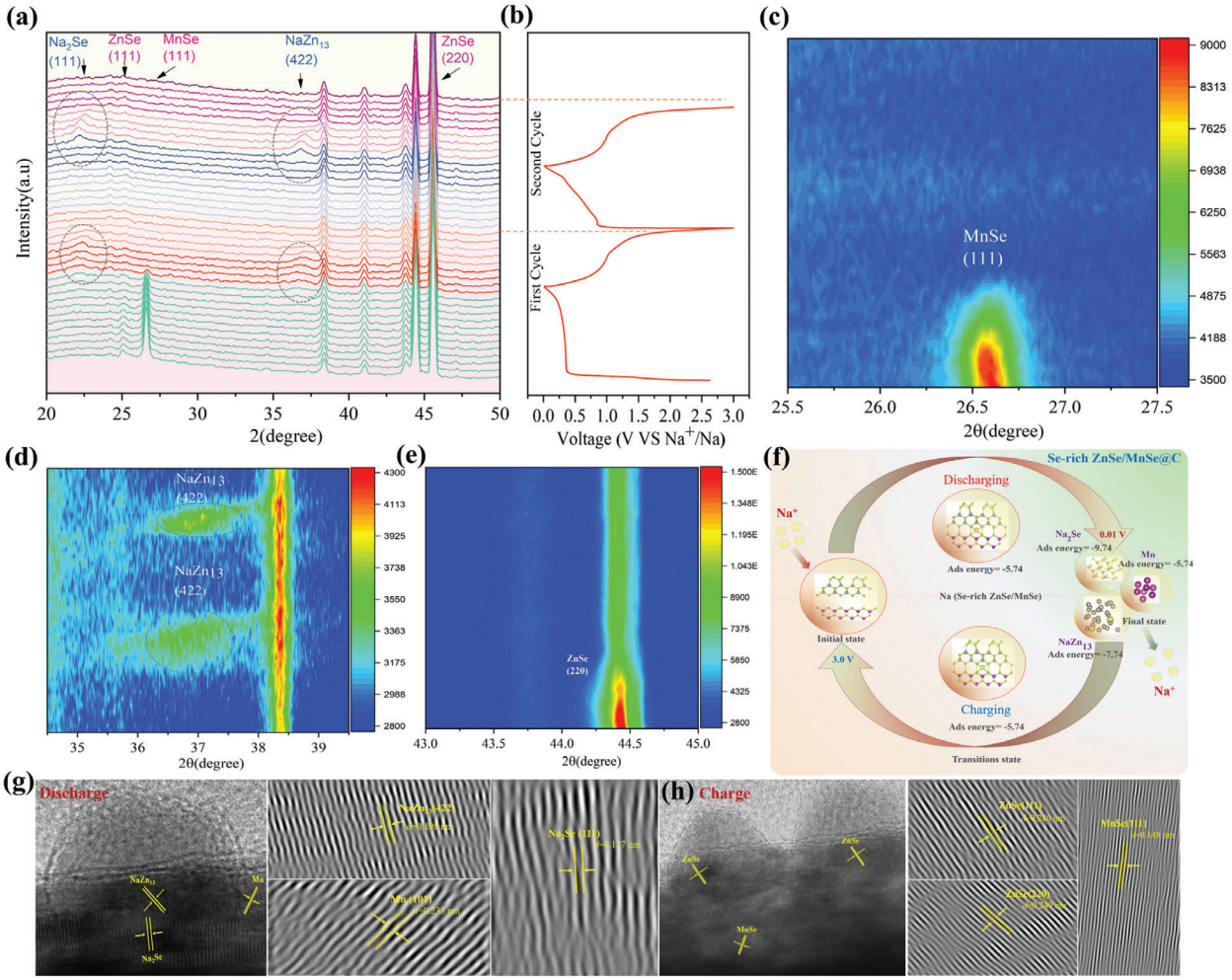

Figure 4. Electrochemical conversion reaction analysis: a–e) In situ XRD patterns of the optimized Se-rich ZnSe/MnSe@C for two consecutive cycles. f) simulation study of the Se-rich ZnSe/MnSe@C electrode during cycling process. g,h) Ex situ HRTEM images discharge to 0.01 V and charge 3.0 V, respectively.

sulfides base anodes,[26] and its characterizations and electrochemical performances are shown in (Figures S29,S30, Supporting Information). The compensation (pre-sodiation) process optimized the electrochemical performance for both anode and cathode in the half cell, simply implying that NVP will showcase the great potency for SIBs. The schematic diagram of the full battery (Se-rich ZnSe/MnSe@C‖ NVP) is displayed in Figure 5a. As expected battery delivered a remarkable initial specific capacity of 248 mAh g^{-1} and maintained 118 mAh g^{-1} at 0.1 A g^{-1} after 60 cycles with a voltage potential of 1.5–4.0 V (Figure 5b). The corresponding GDC profiles of the half-battery anode, cathode, and full battery are depicted in Figure 5c. The full battery also exhibits wonderful rate performance likewise in the half cell of the anode as above (Figure 5d), which shows 246, 143, 79, and 50 mAh g^{-1} at various current densities of 0.1, 0.2, 0.3, and 0.4 A g^{-1}, and the capacity is almost recycled when the current decreases again to 0.1 A g^{-1}. The GDC profiles of the scan rates are shown in Figure 5e. The CV curves at different scan rates are demonstrated in Figure 5f, which present noticeable peak intensities, indicating incredible electrochemical conversion reactions during the cycling process. More precisely, the full battery demonstrates notable long-term cycling performance, delivering 31 mAh g^{-1} at 0.5 A g^{-1} after 400 cycles (Figure 5g). Furthermore, our three full cells at a nominal voltage of 5.50 V brighten the commercial LED with HIC base monogram for a practical approach (Figure 5h).

3. Conclusion

In summary, we present a fundamental principle about tuning the Se-rich particles on the surface of the hexagonal ZnSe/MnSe@C heterostructure to synthesize a highly efficient host for SIBs. DFT investigation demonstrated that the substituting of Se-rich particles in the heterostructure could trigger Zn (e.g., orbitals) near to Fermi level (conduction band) and Mn (e.g., orbitals) away from the conduction band, representing the strong interaction between d–d orbitals. The optimized model structure of Se-rich ZnSe/MnSe@C heterostructure indicated strong d–d interaction between metal orbitals induced the ferromagnetic behavior of MnSe, leading to filling the charge

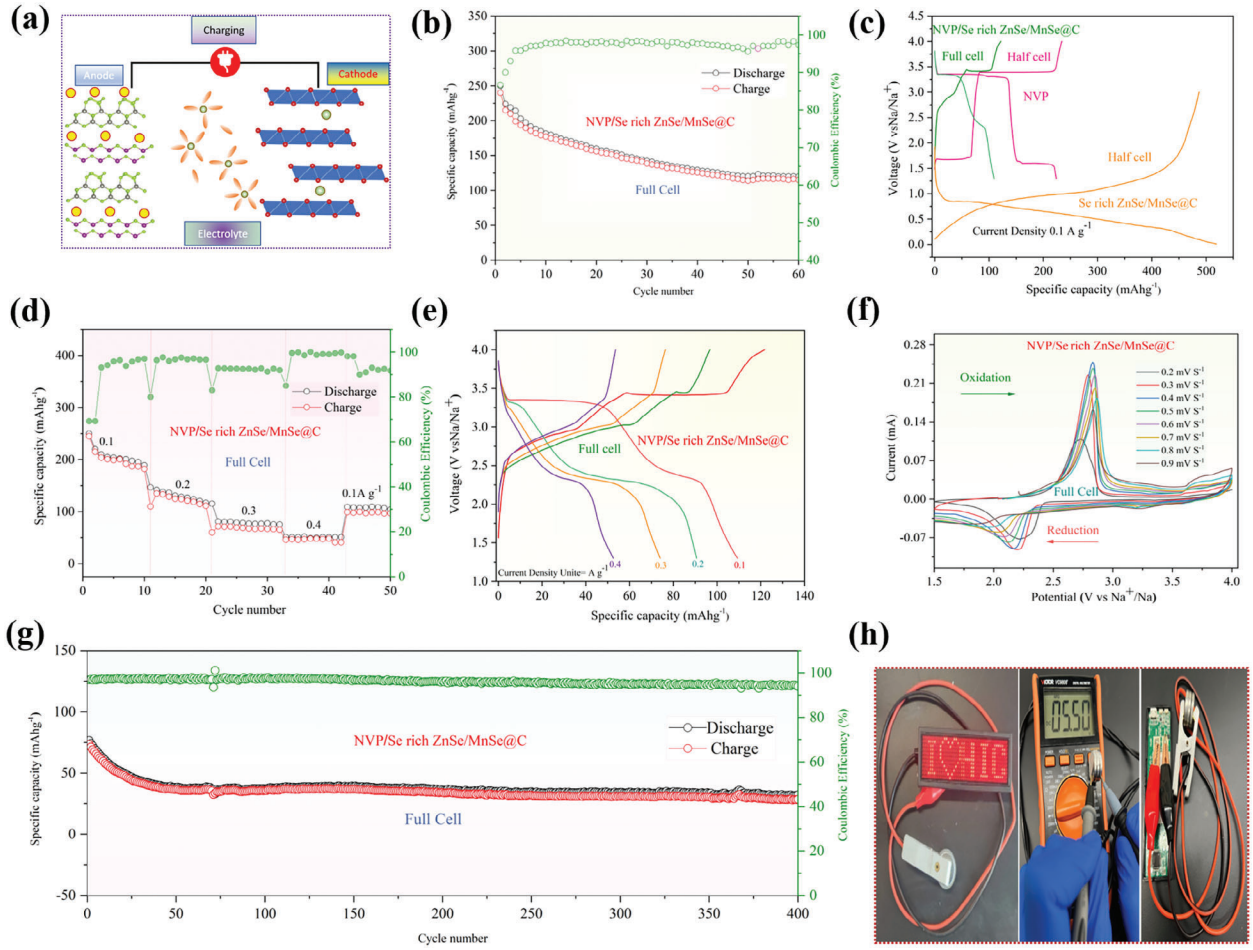

Figure 5. Electrochemical performances of SIBs full cell, a) Schematic model of Se-rich ZnSe/MnSe@C ‖NVP full cell. b) Cycling performance, c) GDC curves of anode, cathode and full cell, d) rate performances, e) GDC curves, and e) CV cycles of the full cell. g) Long cycling performance of the full cell. h) LED lightning by full cell.

transfer more smoothly from ZnSe to MnSe in the heterostructure, therefore, accelerated the Na^+ insertion and de-insertion and facilitated the redox kinetics during the cycling process. Consequently, the optimized Se-rich ZnSe/MnSe@C heterostructure illustrates superior rate capability and excellent long cycling performance, which was even obtained 384 mAh g at 1 A g^{-1} after 2500 cycles. A validity in SIBs full cell tests was also put into practice using optimized Se-rich ZnSe/MnSe@C heterostructure showing tremendous promise for adaptable energy storage devices. The descent structural integrity and reversibility were further measured through in situ XRD, ex situ EIS, and ex situ SEM and HRTEM. We firmly believe that the highlighted significance and understanding of the structure-property interactions of Se-rich ZnSe/MnSe@C heterostructure would encourage the electrochemical conversion kinetics to unlock the Na ion storage domains.

Supporting Information

Supporting Information is available from the Wiley Online Library or from the author.

Acknowledgements

This work was supported by the National Key R&D Program (2022YFB2502000), the National Natural Science Foundation of China for International Young Scientists (22350410379), the Zhejiang Provincial Natural Science Foundation of China (LZ23B030003), the Fundamental Research Funds for the Central Universities (2021FZZX001), and Ten Thousand Talent Program of Zhejiang Province. Moreover, M. B. Hussain and J. Rehman assisted in revising the manuscript.

Conflict of interest

The authors declare no conflict of interest.

Author Contributions

S.I., Y.J., and M.Y. conceived the idea. S.I. designed the experiments and performed the synthesis, physical characterization and electrochemical measurements. S.I. and M.Y. co-wrote and revised the manuscript. A.N.C., Y.H., X.W., W.L., and M.Y. participated in the scientific result discussions. All the authors contributed to the overall scientific interpretation.

Data Availability Statement

The data that support the findings of this study are available from the corresponding author upon reasonable request.

Keywords

d–d orbitals interaction, high reversibility, Se-p orbitals, Se-rich ZnSe/MnSe@C, sodium-ion storage

Received: September 19, 2023
Revised: January 16, 2024
Published online:

[1] a) C. Vaalma, D. Buchholz, M. Weil, S. Passerini, *Nat. Rev. Mater.* **2018**, *3*, 18013; b) M. Yousaf, U. Naseer, A. Imran, Y. Li, W. Aftab, A. Mahmood, N. Mahmood, X. Zhang, P. Gao, Y. Lu, S. Guo, H. Pan, Y. Jiang, *Mater. Today* **2022**, *58*, 238; c) M. Yousaf, U. Naseer, Y. Li, Z. Ali, N. Mahmood, L. Wang, P. Gao, S. Guo, *Energy Environ. Sci.* **2021**, *14*, 2670; d) Y. Jin, P. M. L. Le, P. Gao, Y. Xu, B. Xiao, M. H. Engelhard, X. Cao, T. D. Vo, J. Hu, L. Zhong, B. E. Matthews, R. Yi, C. Wang, X. Li, J. Liu, J.-G. Zhang, *Nat. Energy* **2022**, *7*, 718; e) M. Yousaf, Y. Wang, Y. Chen, Z. Wang, A. Firdous, Z. Ali, N. Mahmood, R. Zou, S. Guo, R. P. S. Han, *Adv. Energy Mater.* **2019**, *9*, 1900567; f) M. Yousaf, H. T. H. Shi, Y. Wang, Y. Chen, Z. Ma, A. Cao, H. E. Naguib, R. P. S. Han, *Adv. Energy Mater.* **2016**, *6*, 1600490.

[2] a) M. Li, J. Lu, X. Ji, Y. Li, Y. Shao, Z. Chen, C. Zhong, K. Amine, *Nat. Rev. Mater.* **2020**, *5*, 276; b) M. Yousaf, Z. Wang, Y. Wang, Y. Chen, U. Ali, M. Maqbool, A. Imran, N. Mahmood, P. Gao, R. P. S. Han, *Small* **2020**, *16*, 2002200; c) Y. Katsuyama, A. Kudo, H. Kobayashi, J. Han, M. Chen, I. Honma, R. B. Kaner, *Small* **2022**, *18*, 2202277. d) Y. Fang, D. Luan, Y. Chen, S. Gao, X. W. Lou, *Angew. Chem., Int. Ed.* **2020**, *59*, 2644. e) X. Chen, N. Sawut, K. Chen, H. Li, J. Zhang, Z. Wang, M. Yang, G. Tang, X. Ai, H. Yang, Y. Fang, Y. Cao, *Energy Environ. Sci.* **2023**, *16*, 4041.

[3] a) B. Zhang, R. Dugas, G. Rousse, P. Rozier, A. M. Abakumov, J.-M. Tarascon, *Nat. Commun.* **2016**, *7*, 10308. b) L. Xiao, F. Ji, J. Zhang, X. Chen, Y. Fang, *Small* **2023**, *19*, 2205732. c) S. Iqbal, L. Wang, Z. Kong, Y. Zhai, X. Sun, F. Wang, Z. Jing, X. He, J. Dou, L. Xu, *ACS Appl. Mater. Interfaces* **2022**, *14*, 15324. d) X. Sun, L. Wang, C. Li, D. Wang, I. Sikandar, R. Man, F. Tian, Y. Qian, L. Xu, *Nano Res.* **2021**, *14*, 4696.

[4] Y. Liu, X. Hu, J. Li, G. Zhong, J. Yuan, H. Zhan, Y. Tang, Z. Wen, *Nat. Commun.* **2022**, *13*, 663.

[5] a) Z. Hu, Q. Liu, S.-L. Chou, S.-X. Dou, *Adv. Mater.* **2017**, *29*, 1700606; b) T. Liu, Y. Yang, S. Cao, R. Xiang, L. Zhang, J. Yu, *Adv. Mater.* **2023**, *35*, 2207752; c) H. He, H. Zhang, D. Huang, W. Kuang, X. Li, J. Hao, Z. Guo, C. Zhang, *Adv. Mater.* **2022**, *34*, 2200397; d) Z. Kong, L. Wang, S. Iqbal, B. Zhang, B. Wang, J. Dou, F. Wang, Y. Qian, M. Zhang, L. Xu, *Small* **2022**, *18*, 2107252; e) M. Yousaf, Y. Chen, H. Tabassum, Z. Wang, Y. Wang, A. Y. Abid, A. Mahmood, N. Mahmood, S. Guo, R. P. S. Han, P. Gao, *Adv. Sci.* **2020**, *7*, 1902907.

[6] H. Shan, J. Qin, Y. Ding, H. M. K. Sari, X. Song, W. Liu, Y. Hao, J. Wang, C. Xie, J. Zhang, X. Li, *Adv. Mater.* **2021**, *33*, 2102471.

[7] Q. Pan, Z. Tong, Y. Su, Y. Zheng, L. Shang, Y. Tang, *Adv. Mater.* **2022**, *34*, 2203485.

[8] G. Fang, Q. Wang, J. Zhou, Y. Lei, Z. Chen, Z. Wang, A. Pan, S. Liang, *ACS Nano* **2019**, *13*, 5635.

[9] Y. Xiao, H.-R. Wang, H.-Y. Hu, Y.-F. Zhu, S. Li, J.-Y. Li, X.-W. Wu, S.-L. Chou, *Adv. Mater.* **2022**, *34*, 2202695.

[10] H. Huang, R. Xu, Y. Feng, S. Zeng, Y. Jiang, H. Wang, W. Luo, Y. Yu, *Adv. Mater.* **2020**, *32*, 1904320.

[11] a) J. Yang, X. Zhou, D. Wu, X. Zhao, Z. Zhou, *Adv. Mater.* **2017**, *29*, 1604108; b) Y. Li, J. Qian, M. Zhang, S. Wang, Z. Wang, M. Li, Y. Bai, Q. An, H. Xu, F. Wu, L. Mai, C. Wu, *Adv. Mater.* **2020**, *32*, 2005802; c) D. Yuan, Y. Dou, Y. Tian, D. Adekoya, L. Xu, S. Zhang, *Angew. Chem., Int. Ed.* **2021**, *60*, 18830; d) Q. Wang, Y. Liao, X. Jin, C. Cheng, S. Chu, C. Sheng, L. Zhang, B. Hu, S. Guo, H. Zhou, *Angew. Chem., Int. Ed.* **2022**, *61*, e202206625.

[12] T. Yang, M. Fang, J. Liu, D. Yang, Y. Liang, J. Zhong, Y.-J. Yuan, Y. Zhang, X. Liu, R. Zheng, K. Davey, J. Zhang, Z. Guo, *Adv. Funct. Mater.* **2022**, *32*, 2205880.

[13] Y. Jiang, Y.-P. Deng, R. Liang, J. Fu, R. Gao, D. Luo, Z. Bai, Y. Hu, A. Yu, Z. Chen, *Nat. Commun.* **2020**, *11*, 5858.

[14] G. Assat, J.-M. Tarascon, *Nat. Energy* **2018**, *3*, 373.

[15] C. Wang, L. Liu, S. Zhao, Y. Liu, Y. Yang, H. Yu, S. Lee, G.-H. Lee, Y.-M. Kang, R. Liu, F. Li, J. Chen, *Nat. Commun.* **2021**, *12*, 2256.

[16] a) K. Liu, X. Ma, S. Xu, Y. Li, M. Zhao, *npj Comput. Mater.* **2023**, *9*, 16; b) Q. Bai, L. Yang, H. Chen, Y. Mo, *Adv. Energy Mater.* **2018**, *8*, 1702998.

[17] H. Shan, J. Qin, J. Wang, H. M. K. Sari, L. Lei, W. Xiao, W. Li, C. Xie, H. Yang, Y. Luo, G. Zhang, X. Li, *Adv. Sci.* **2022**, *9*, 2200341.

[18] a) C. F. Dong, L. Q. Wu, Y. Y. He, Y. L. Zhou, X. P. Sun, W. Du, X. Q. Sun, L. Q. Xu, F. Y. Jiang, *Small* **2020**, *16*, 2004580; b) J. Wang, B. Wang, X. Liu, J. Bai, H. Wang, G. Wang, *Chem. Eng. J.* **2020**, *382*, 123050.

[19] Z. Ye, Y. Jiang, L. Li, F. Wu, R. Chen, *Adv. Mater.* **2021**, *33*, 2101204.

[20] T. Li, Y. Wang, L. Yuan, Q. Zhou, S. Qiao, Z. Liu, S. Chong, *Chem. Eng. J.* **2022**, *446*, 137152.

[21] C. Yang, X. Liang, X. Ou, Q. Zhang, H.-S. Zheng, F. Zheng, J.-H. Wang, K. Huang, M. Liu, *Adv. Funct. Mater.* **2019**, *29*, 1807971.

[22] X. Chen, M. Li, S.-P. Wang, C. Wang, Z. Shen, F.-Q. Bai, F. Du, *Adv. Sci.* **2022**, *9*, 2104630.

[23] Y. Wu, C. Zhang, H. Zhao, Y. Lei, *J. Mater. Chem. A* **2021**, *9*, 9506.

[24] D. Chao, P. Liang, Z. Chen, L. Bai, H. Shen, X. Liu, X. Xia, Y. Zhao, S. V. Savilov, J. Lin, Z. X. Shen, *ACS Nano* **2016**, *10*, 10211.

[25] a) D. Cao, W. Kang, W. Wang, K. Sun, Y. Wang, P. Ma, D. Sun, *Small* **2020**, *16*, 1907641; b) J. Xie, X. Li, H. Lai, Z. Zhao, J. Li, W. Zhang, W. Xie, Y. Liu, W. Mai, *Angew. Chem., Int. Ed.* **2019**, *58*, 14740.

[26] J. Cao, L. Wang, D. Li, Z. Yuan, H. Xu, J. Li, R. Chen, V. Shulga, G. Shen, W. Han, *Adv. Mater.* **2021**, *33*, 2101535.